

Transverse phase space characterisation in the CLARA FE accelerator test facility at Daresbury Laboratory

A. Wolski* and D.C. Christie

University of Liverpool, Liverpool, UK, and the Cockcroft Institute, Daresbury, UK.

B.L. Militsyn, D.J. Scott, and H. Kockelbergh
STFC/ASTeC, Daresbury Laboratory, Daresbury, UK.

(Dated: October 24, 2019)

We compare three techniques for characterising the transverse phase space distribution of the beam in CLARA FE (the Compact Linear Accelerator for Research and Applications Front End, at Daresbury Laboratory, UK): emittance and optics measurements using screens at three separate beamline locations; quadrupole scans; and phase space tomography. We find that where the beam distribution has significant structure (as in the case of CLARA FE at the time the measurements presented here were made) tomography analysis is the most reliable way to obtain a meaningful characterisation of the transverse beam properties. We present the first experimental results from four-dimensional phase space tomography: our results show that this technique can provide an insight into beam properties that are of importance for optimising machine performance.

I. INTRODUCTION

Knowledge of transverse beam emittance and optical properties are essential for the commissioning and performance optimisation of many accelerator facilities. There are well-established techniques for emittance and optics measurements, often based on observation of changes in beam size in response to changes in strength of focusing (quadrupole) magnets, or observation of the beam size at different locations along a beam line [1, 2]. Beam phase space tomography is also an established method for providing detailed information about the phase space distribution [3–10]. In this paper, we report the results of studies on CLARA FE (Compact Linear Accelerator for Research and Applications, Front End) at Daresbury Laboratory [11, 12], aimed at characterising the transverse emittance and optical properties of the electron beam. The results of three different measurement techniques are compared, namely: beam-size measurements at three different locations along the beamline (“three-screen analysis”); measurement in the change of the beam size in response to the change in quadrupole strengths (“quadrupole scan”); and beam phase space tomography, with which we demonstrate for the first time reconstruction of the four-dimensional transverse phase space. At the time that the studies were carried out, the beam in CLARA FE had significant detailed structure in the phase space distribution (i.e. the phase space distribution could not be described by a simple Gaussian). We find that in these circumstances, phase space tomography provides the most reliable characterisation of the transverse beam properties. Quadrupole scans can provide some useful information, but the results from three-screen analysis can be unreliable. Our studies of phase

space tomography include the first experimental demonstration of beam tomography in four-dimensional phase space [13, 14]. We find that this technique can provide an insight into coupling in the beam, which can be of value for optimising machine performance [15].

This paper is organised as follows. In Section II we briefly review the definitions that we use for the emittances and optics functions in coupled beams, and the methods that we use for calculating these quantities. In Section III we describe the measurement procedures in CLARA FE. The three-screen analysis method is discussed in Section III A, where simulation and experimental results for a single measurement case are presented. The results show some limitations of the technique, and we discuss in particular why it does not produce reliable results when the beam has a complicated structure in phase space (i.e. the distribution is not a simple Gaussian). In Section III B we describe the quadrupole scan analysis method, including application to measurement of the full covariance matrix in two (transverse) degrees of freedom. The quadrupole scan technique has some advantages over the three-screen analysis, but neither method can determine the detailed structure of the beam distribution in phase space. Such information can be provided by the final analysis technique, phase space tomography, which is considered in Section III C. We describe the phase space tomography technique, including the use of normalised phase space [16], and show how tomography can be applied to determine the beam distribution in four-dimensional phase space [14]. Simulation results are presented to validate the technique, and some experimental results are again presented. In Section IV we show the application of phase space tomography to provide a detailed characterisation of the beam in CLARA FE under a range of machine conditions, looking at the dependence of emittance and optics (including coupling) on strength of the electron source solenoid, bucking coil, and bunch charge. Given the detailed structure generally present in the phase space distribution of the beam,

*Electronic address: a.wolski@liverpool.ac.uk

phase space tomography provides important insights into the beam properties and behaviour that would not be obtained from the three-screen or quadrupole scan analysis techniques. Tomography in four-dimensional phase space provides, in particular, information on beam coupling that is of value for optimising machine performance. Finally, in Section V, we summarise the key results, discuss the main conclusions, and consider appropriate directions for further work.

II. NORMAL MODE EMITTANCES AND OPTICAL FUNCTIONS

Since various definitions of beam emittance are used in different contexts, we briefly review the definition we use for the studies presented here, considering in particular the case where there is coupling in the beam. For clarity, however, we begin with the case of a single degree of freedom. Considering, for example, the transverse horizontal direction, the covariance matrix at a specified point in a beamline can be written:

$$\Sigma = \begin{pmatrix} \langle x^2 \rangle & \langle xp_x \rangle \\ \langle xp_x \rangle & \langle p_x^2 \rangle \end{pmatrix}, \quad (1)$$

where x represents the transverse horizontal co-ordinate of a single particle at the specified location, p_x is the horizontal momentum P_x (at the same location) divided by a chosen reference momentum P_0 , and the brackets $\langle \rangle$ indicate an average over all particles in the beam. Note that we assume there is no dispersion in the beamline, so that the trajectory of the beam (nominally passing through the centre of each quadrupole) is independent of its energy: for the present studies in CLARA FE, since the layout from the electron source to the end of the section where the emittance measurements are performed is a straight line, this will be a good approximation.

The horizontal (geometric) emittance ϵ_x and optical functions (Courant–Snyder parameters β_x and α_x and γ_x) can be calculated from:

$$\epsilon_x = \sqrt{\langle x^2 \rangle \langle p_x^2 \rangle - \langle xp_x \rangle^2}, \quad (2)$$

$$\beta_x = \frac{\langle x^2 \rangle}{\epsilon_x}, \quad (3)$$

$$\alpha_x = -\frac{\langle xp_x \rangle}{\epsilon_x}, \quad (4)$$

$$\gamma_x = \frac{\langle p_x^2 \rangle}{\epsilon_x}. \quad (5)$$

These relations imply that:

$$\gamma_x \langle x^2 \rangle + 2\alpha_x \langle xp_x \rangle + \beta_x \langle p_x^2 \rangle = 2\epsilon_x. \quad (6)$$

Equation (6) defines an “emittance ellipse” in phase space. It is straightforward to extend these results to the vertical direction, to find the vertical emittance and Courant–Snyder parameters.

In considering only a single degree of freedom, we assume that there is no transverse coupling in the beam or in the beamline, so that the transverse horizontal and vertical motions may be treated independently. Coupling in the beam will be characterised by non-zero values for cross-plane elements (such as $\langle xy \rangle$, for example) in the 4×4 covariance matrix. Coupling in the beamline will arise from skew components in the quadrupoles (for example, from some alignment error in the form of a tilt of the magnet around the beam axis) or from a solenoid field either at the source or further down the beamline. If there is coupling in the beam, then the emittance calculated using (2) will not be the most useful quantity, since it will not be constant as the beam travels along the beamline. The conserved quantities where coupling is present are the normal mode emittances (or eigen-emittances) ϵ_I and ϵ_{II} , where $\pm i\epsilon_{I,II}$ are the eigenvalues of ΣS , with Σ the 4×4 covariance matrix, and S the antisymmetric matrix:

$$S = \begin{pmatrix} 0 & 1 & 0 & 0 \\ -1 & 0 & 0 & 0 \\ 0 & 0 & 0 & 1 \\ 0 & 0 & -1 & 0 \end{pmatrix}. \quad (7)$$

Various formalisms have been developed for generalising the emittance and Courant–Snyder parameters from one to two (or more) coupled degrees of freedom. Here, we use the method presented in [17], in which the (i, j) element of a covariance matrix Σ is related to the normal mode emittances ϵ_I , ϵ_{II} and corresponding optical functions β_{ij}^I , β_{ij}^{II} by:

$$\Sigma_{ij} = \sum_{k=I,II} \epsilon_k \beta_{ij}^k. \quad (8)$$

The optical functions can be obtained from the eigenvectors of ΣS . If U is a matrix constructed from the eigenvectors (arranged in columns) of ΣS , then:

$$\Sigma S = U \Lambda U^{-1}, \quad (9)$$

where Λ is a diagonal matrix with diagonal elements corresponding to the eigenvalues of ΣS . If the eigenvectors and eigenvalues are arranged so that, in two degrees of freedom:

$$\Lambda = \begin{pmatrix} -i\epsilon_I & 0 & 0 & 0 \\ 0 & i\epsilon_I & 0 & 0 \\ 0 & 0 & -i\epsilon_{II} & 0 \\ 0 & 0 & 0 & i\epsilon_{II} \end{pmatrix}, \quad (10)$$

then the optical functions are given by:

$$\beta^k = U E^k U^{-1} S, \quad (11)$$

where $k = I, II$, and:

$$E^I = \begin{pmatrix} i & 0 & 0 & 0 \\ 0 & -i & 0 & 0 \\ 0 & 0 & 0 & 0 \\ 0 & 0 & 0 & 0 \end{pmatrix}, \quad E^{II} = \begin{pmatrix} 0 & 0 & 0 & 0 \\ 0 & 0 & 0 & 0 \\ 0 & 0 & i & 0 \\ 0 & 0 & 0 & -i \end{pmatrix}. \quad (12)$$

The covariance matrix Σ can then be expressed in terms of the normal mode emittances and optical functions using (8).

When there is no coupling, the normal mode emittances and optical functions correspond to the usual quantities defined for independent degrees of freedom. For example, where the transverse horizontal motion is independent of the vertical and longitudinal motion, then:

$$\epsilon_I = \sqrt{\langle x^2 \rangle \langle p_x^2 \rangle - \langle xp_x \rangle^2} = \epsilon_x, \quad (13)$$

and:

$$\beta_{1,1}^I = \beta_x, \quad \text{and} \quad \beta_{1,2}^I = -\alpha_x. \quad (14)$$

Finally, we note that if the optical functions β_{ij}^k at a given point s_1 in a beamline are known, the optical functions at any other point s_2 are readily computed using:

$$\beta_{ij}^k(s_2) = M_{21} \beta_{ij}^k(s_1) M_{21}^T, \quad (15)$$

where M_{21} is the transfer matrix from s_1 to s_2 (calculated, for example, from a computational model of the beamline). The normal mode emittances and optical functions defined as described here, therefore provide convenient quantities for describing the variation of the beam sizes $\langle x^2 \rangle$, $\langle y^2 \rangle$ (and other elements of the covariance matrix) along a given beamline.

III. MEASUREMENTS IN CLARA FE

Ultimately, CLARA is planned as a facility that will provide a high-quality electron beam with energy up to 250 MeV for scientific and medical research, and for the development of new accelerator technologies including (with the addition of an undulator section) the testing of advanced techniques and novel modes of FEL operation. So far, only the front end (CLARA FE) has been constructed: this consists of a low-emittance rf photocathode electron source and a linac reaching 35.5 MeV/c beam momentum. The layout of CLARA FE is shown in Fig. 1. The electron source [18] consists of a 2.5 cell S-band rf cavity with copper photocathode, and can deliver short (of order a few ps) bunches at 10 Hz repetition rate with charge in excess of 250 pC and with beam momentum up to 5.0 MeV/c. The source is driven with the third harmonic of a short (2 ps full-width at half maximum) pulsed Ti:Sapphire laser with a pulse energy of up to 100 μ J. The typical size of the laser spot on the photocathode is of order 600 μ m. The source is immersed in the field of a solenoid magnet which provides emittance compensation and focusing of the beam in the initial section of the beamline. A bucking coil located beside the source cancels the field from the solenoid on the photocathode in the region of the laser spot.

The studies reported in this paper are based on measurements made in the section of CLARA FE following

the linac, at a nominal beam momentum of 30 MeV/c. Measurements were made under a range of conditions including various bunch charges, and different strengths of the solenoid and bucking coil at the electron source. Three techniques were used, to allow a comparison of the results and evaluation of the benefits and limitations of the different methods. The first technique, the three-screen measurement and analysis method (described in more detail in Section III A, below), is based on observations of the transverse beam profile at three scintillating (YAG) screens, shown as SCR-01, SCR-02 and SCR-03 in Fig. 1. The quadrupole scan (Section III B) and tomography (Section III C) methods use only observations of the beam on SCR-03, though observations on SCR-02 were also made, and used to validate the results. For each of the three methods, two quadrupoles (QUAD-01 and QUAD-02) between the end of the linac and SCR-01 were used for setting the optical functions of the beam on SCR-01, and were kept at fixed strengths during data collection. A collimator is located between SCR-01 and SCR-02, but this was not used during the measurements. For all three measurement techniques, the strengths of three quadrupoles (QUAD-03, QUAD-04 and QUAD-05 in Fig. 1) located between SCR-02 and SCR-03 were varied. For the three-screen analysis, only the beam sizes for one set of magnet strengths are strictly needed to calculate the emittances and optical functions; however, as described in Section III A, measurements with different sets of quadrupole strengths can be used to validate the results by showing the consistency for emittance and optics values obtained for different strengths.

In the case of the quadrupole scan and tomography methods, SCR-03 provides the necessary data, and is referred to as the ‘‘Observation Point’’. For ease of comparison, for all three techniques we construct the covariance matrix at SCR-02, which is referred to as the ‘‘Reconstruction Point’’.

At each point in a quadrupole scan on CLARA FE, ten screen images were recorded on successive machine pulses (at a rate of 10 Hz, with a single bunch per pulse): this allows an estimate to be made of random errors arising from pulse-to-pulse variations in beam properties. A background image was recorded without beam (i.e. with the photocathode laser blocked), so that any constant artefacts in the beam images, for example from dark current, could be subtracted. The rms beam sizes were calculated by projecting the image onto either the x or y axis, with co-ordinates measured with respect to a centroid such that:

$$\langle x \rangle = \langle y \rangle = 0. \quad (16)$$

Average quantities are calculated from a beam image by integration of the image intensity with an appropriate weighting, for example:

$$\langle x \rangle = \frac{\iint x I(x, y) dx dy}{\iint I(x, y) dx dy}, \quad (17)$$

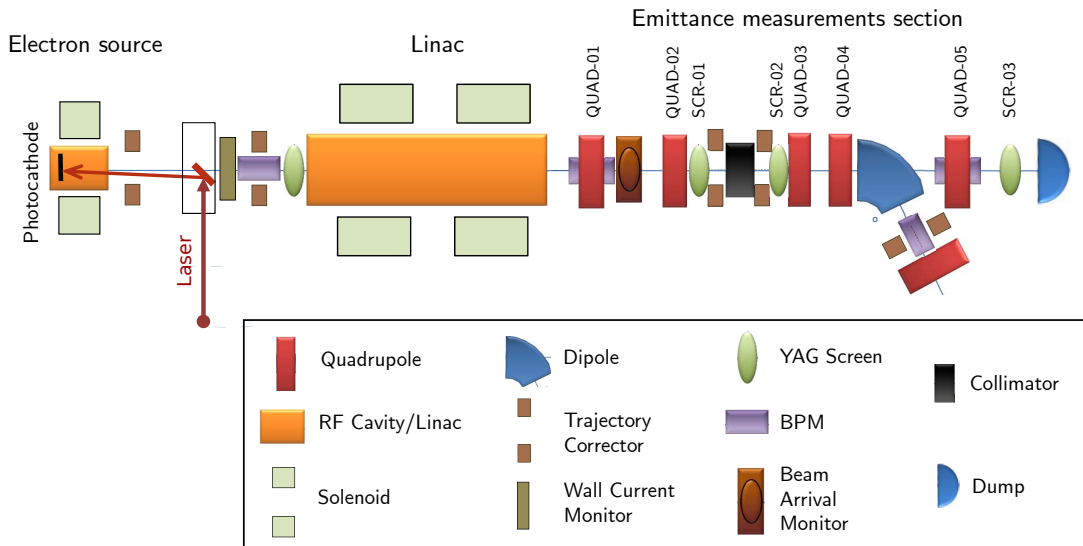


FIG. 1: Layout of CLARA FE (not to scale), showing the electron source, magnetic elements, linac, and diagnostics. For the emittance measurements, quadrupoles QUAD-01 and QUAD-02 were used to set the required optics at screen SCR-01. For each measurement, beam images on SCR-03 (the Observation Point) were recorded for different strengths of quadrupoles QUAD-03, QUAD-04 and QUAD-05. The optical functions and phase space distribution were computed at SCR-02 (the Reconstruction Point). Screens SCR-01, SCR-02 and SCR-03 are 0.61 m, 1.53 m and 3.20 m from the entrance of QUAD-01, respectively.

where $I(x, y)$ is the image intensity at a given point on the screen.

Between each quadrupole scan, the quadrupole magnets were cycled over a set range of strengths to minimise systematic errors from hysteresis. Remaining sources of systematic errors include calibration factors for the magnets (when converting from coil currents to field gradients), magnet fringe fields, calibration factors for the screens, and accelerating gradient in the linac. It was found that better agreement between the analysis results and direct observations (used to validate the results) could be obtained if the beam momentum in the model used in the analysis was reduced slightly from the nominal 30 MeV/c. In the results presented here, a momentum of 29.5 MeV/c is used. It should also be noted that some variation in machine parameters (including rf phase and amplitude in the electron source and the linac) is likely to have occurred during data collection, and because of the time required to re-tune the machine it was not always possible to confirm all the parameter values between quadrupole scans.

In principle, for each of the three measurement and analysis methods, the strengths of the quadrupoles between SCR-02 and SCR-03 can be chosen randomly. However, if the profile of the beam on any of the screens becomes too large, too small, or very asymmetric (with large aspect ratio) then there can be a large error in the calculation of the rms beam size. Before collecting data, therefore, simulations were performed to find sets of magnet strengths, with fixed QUAD-01 and QUAD-02 and variable QUAD-03, QUAD-04 and QUAD-05, for which the transverse beam profiles on each of the three screens would remain approximately circular, and with a con-

venient size. It is also worth noting that, from (2), a large value of α_x at a given location can indicate a large value for $\langle xp_x \rangle$ at that location: calculation of the emittance then involves taking the difference between quantities that may be of similar magnitude, leading to a large uncertainty in the result. A further constraint, therefore, was to find strengths for QUAD-01 and QUAD-02 that would provide a beam waist in x and y (i.e. with α_x and α_y close to zero) at SCR-02 (the Reconstruction Point). Finally, quadrupole strengths were chosen to provide a wide range of horizontal and vertical phase advances from SCR-02 to SCR-03: this is a consideration for the tomographic analysis, and is discussed further in Section III C. Simulations to find sets of suitable strengths for all five quadrupoles were carried out in GPT [19], tracking particles from the photocathode (with nominal laser spot size and pulse length) to SCR-03, using machine conditions matching those planned for the experiments. Space charge effects were included [20, 21], though these effects are only really significant at low momentum, upstream of the linac.

A. Three-screen method

The three-screen analysis method is based on the principle that, given the rms beam size (in either the transverse horizontal or vertical direction) at three separate locations, and knowing the transfer matrices between those locations, it is possible to calculate the covariance matrix characterising the phase space beam distribution.

If the transfer matrix from one location in the beamline s_1 to another location s_2 is M_{21} (with transpose M_{21}^T),

then:

$$\Sigma_2 = M_{21}\Sigma_1M_{21}^T, \quad (18)$$

where Σ_1 is the covariance matrix at s_1 and Σ_2 is the covariance matrix at s_2 . Similarly, at a third location s_3 :

$$\Sigma_3 = M_{32}\Sigma_2M_{32}^T, \quad (19)$$

where Σ_3 is the covariance matrix at s_3 , and M_{32} is the transfer matrix from s_2 to s_3 . The elements of the transfer matrices can be calculated using a linear model of the beamline, with known quadrupole strengths.

Given measured values of $\langle x_1^2 \rangle$, $\langle x_2^2 \rangle$ and $\langle x_3^2 \rangle$ (from observation of the beam images on the three screens), using (18) and (19) we can find $\langle x_2p_{x2} \rangle$ and $\langle p_{x2}^2 \rangle$ from:

$$\begin{aligned} \langle x_2p_{x2} \rangle &= -\frac{b_{32}\langle x_1^2 \rangle + C_+C_-\langle x_2^2 \rangle - b_{21}^2\langle x_3^2 \rangle}{2C_-b_{21}b_{32}}, \quad (20) \\ \langle p_{x2}^2 \rangle &= \frac{a_{32}b_{32}\langle x_1^2 \rangle + C_-a_{21}a_{32}\langle x_2^2 \rangle - a_{21}b_{21}\langle x_3^2 \rangle}{C_-b_{21}b_{32}}, \quad (21) \end{aligned}$$

where a_{21} and b_{21} are (respectively) the (1, 1) and (1, 2) elements of M_{21}^{-1} , a_{32} and b_{32} are (respectively) the (1, 1) and (1, 2) elements of M_{32} , and:

$$C_{\pm} = a_{32}b_{21} \pm a_{21}b_{32}. \quad (22)$$

In principle, the three-screen analysis method can be extended to construct the 4×4 covariance matrix describing the beam distribution in two transverse degrees of freedom. However, the 4×4 covariance matrix has ten independent elements, while observation of the beam profile on screens at three separate locations provides only nine observable quantities ($\langle x^2 \rangle$, $\langle xy \rangle$ and $\langle y^2 \rangle$ at each screen). Therefore, using observations of the beam profile at three screens does not provide sufficient information to determine all elements of the 4×4 covariance matrix at any point in the beamline, and it is not possible, without additional measurements, to calculate the normal mode emittances. The normal mode emittances can be calculated if observations are made with different sets of quadrupole strengths between the screens (see, for example, [22, 23]): we return to this point in the discussion of the quadrupole scan technique in Section III B. Alternatively, measurements can be made at additional longitudinal positions [24]. Measurements of the 4×4 covariance matrix (for picometer-scale emittance beams) using measurements at multiple longitudinal locations were recently reported by Ji et al. [10].

In the case of CLARA FE, we apply the three-screen analysis technique in horizontal and vertical degrees of freedom separately (neglecting any coupling), with s_1 , s_2 and s_3 corresponding to the locations of screens SCR-01, SCR-02 and SCR-03 respectively (see Fig. 1). Results may be validated by repeating the measurements for different strengths of the three quadrupoles between screens SCR-02 and SCR-03: since the magnets upstream

of SCR-02 remain at constant strength, measurements for different strengths of downstream magnets should all yield the same values for the emittances and Courant–Snyder parameters at this screen.

Figure 2 shows a typical set of results from the three-screen analysis, for the transverse horizontal and vertical directions, respectively. Elements of the covariance matrix scaled by the appropriate Courant–Snyder parameter are plotted as a function of the phase advance from SCR-02 to SCR-03 in the respective plane (corresponding to different strengths of the quadrupoles QUAD-03, QUAD-04 and QUAD-05). In the case of a simple Gaussian distribution with no coupling, from Eqs. (3)–(5) we see that scaling the covariance matrix elements by the Courant–Snyder parameters should give values that are independent of the phase advance, and equal to the geometric emittance. However, the results in Fig. 2 show significant variation in each of the scaled elements of the covariance matrix over the range of the quadrupole scan: this is particularly evident in the horizontal direction, and is reflected in the values calculated for the emittance and optics functions. For the horizontal plane, a significant number of points in the quadrupole scan lead to imaginary values for the emittance (the covariance matrix has negative determinant), or non-physical negative values for the covariance matrix element $\langle p_x^2 \rangle$. Simulation studies, which we discuss further below, suggest that these features result from the non-Gaussian distribution of particles in phase space. Theoretically, this may be understood in terms of the way that the distribution is constructed from observations at the three screens. At each screen, we measure the width of a projection of the phase space distribution onto an axis at a particular phase angle. With three screens, we have projections at three phase angles: if the distribution in phase space is Gaussian, this is sufficient to determine the size and shape of the distribution (which can be described by three parameters; for example, the elements of the covariance matrix, or the emittance and Courant–Snyder parameters). However, a more general distribution with a more complicated structure cannot be described by just three parameters: attempting to do so will lead to different values for those parameters, depending on the particular phase angles chosen for the projections. The results of the tomography analysis presented in Section III C show that at the time that the measurements reported here were made, the beam exhibited a complicated (non-Gaussian) structure in phase space, particularly in the horizontal plane.

We performed simulations to validate the argument that with the three-screen analysis method, the variation in beam parameters for different quadrupole settings arises from the structure of the phase space distribution. In the simulations, we created a set of particles with a given phase space distribution, and tracked the particles (in a computer model of the beamline) from SCR-01 to SCR-02 (the Reconstruction Point) and then to SCR-03. At each screen, the horizontal and vertical rms beam

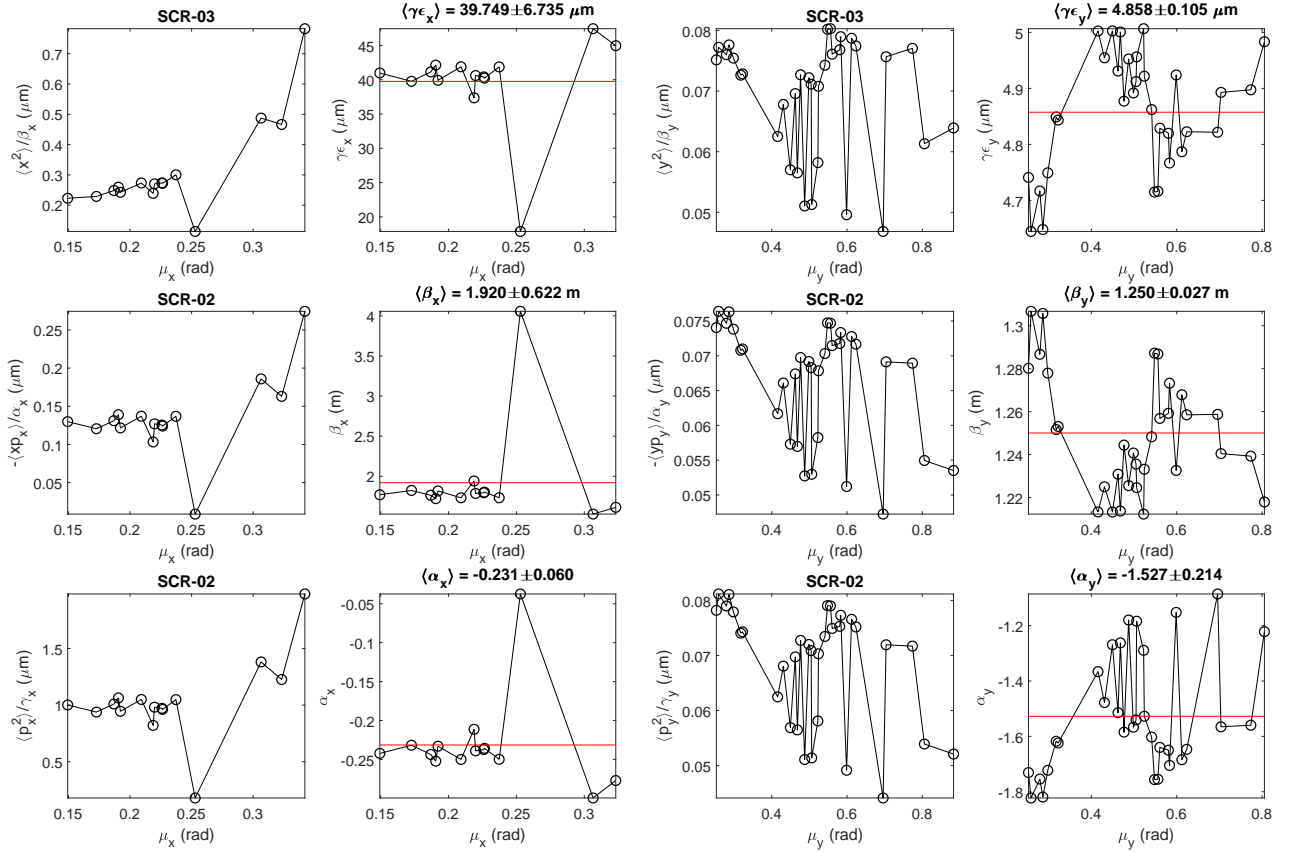


FIG. 2: Horizontal (left two columns) and vertical (right two columns) emittance and optics measurements made using beam images observed at three different locations in the beam line (screens SCR-01, SCR-02 and SCR-03). Each point represents a different set of strengths for the quadrupoles between SCR-02 and SCR-03. The horizontal axis shows the phase advance in the respective plane from SCR-02 to SCR-03; the phase advance from SCR-01 and SCR-02 is fixed. The plots in the first column show (top) $\langle x^2 \rangle / \beta_x$ at SCR-03; (middle) $-\langle xp_x \rangle / \alpha_x$ at SCR-02 calculated from (20); and (bottom) $\langle p_x^2 \rangle / \gamma_x$ at SCR-02 calculated from (21). The plots in the second column show (top) the normalised horizontal emittance; (middle) the horizontal beta function at SCR-02; and (bottom) the horizontal alpha function at SCR-02. The plots in the third and fourth columns correspond to those in the first and second columns, but for the vertical rather than the horizontal plane. The emittance and optical functions are calculated from the covariance matrix at SCR-02, using (2), (3) and (4). Points leading to imaginary values for the emittance are omitted.

size are calculated, and used the same procedure that was applied to the experimental data to calculate the covariance matrix at SCR-02, and the emittance and optical parameters at this point. The tracking and optical calculations are repeated for different strengths of the quadrupoles, corresponding to those used in the experiment. Results for the transverse horizontal plane are shown in Fig. 3. For a Gaussian distribution in phase space, there are only very small variations in the calculated covariance matrix at SCR-02 and in the optical functions, for different quadrupole strengths (the small variations arise from statistical variation in the distribution, resulting from tracking a finite number of particles). The simulation can be repeated, but using instead of a Gaussian distribution, a phase space distribution based on the one found from the tomography study (presented in Section III C). In this case, we see much larger vari-

ations in the covariance matrix at SCR-02 and in the emittance and optical functions at this point, depending on the strengths of the quadrupoles between SCR-02 and SCR-03. For some quadrupole strengths, the calculated covariance matrix is unphysical, and it is not possible to find real values for the emittance or optical functions. The overall behaviour is qualitatively similar in some respects with that seen in the experiment (Fig. 2). Results of simulations for the vertical plane (Fig. 4) again show almost no variation in the emittance or optical functions as a function of quadrupole strength for a Gaussian phase space distribution, but behaviour similar to that observed in experiment in the case of a more realistic phase space distribution based on the results of the tomography analysis.

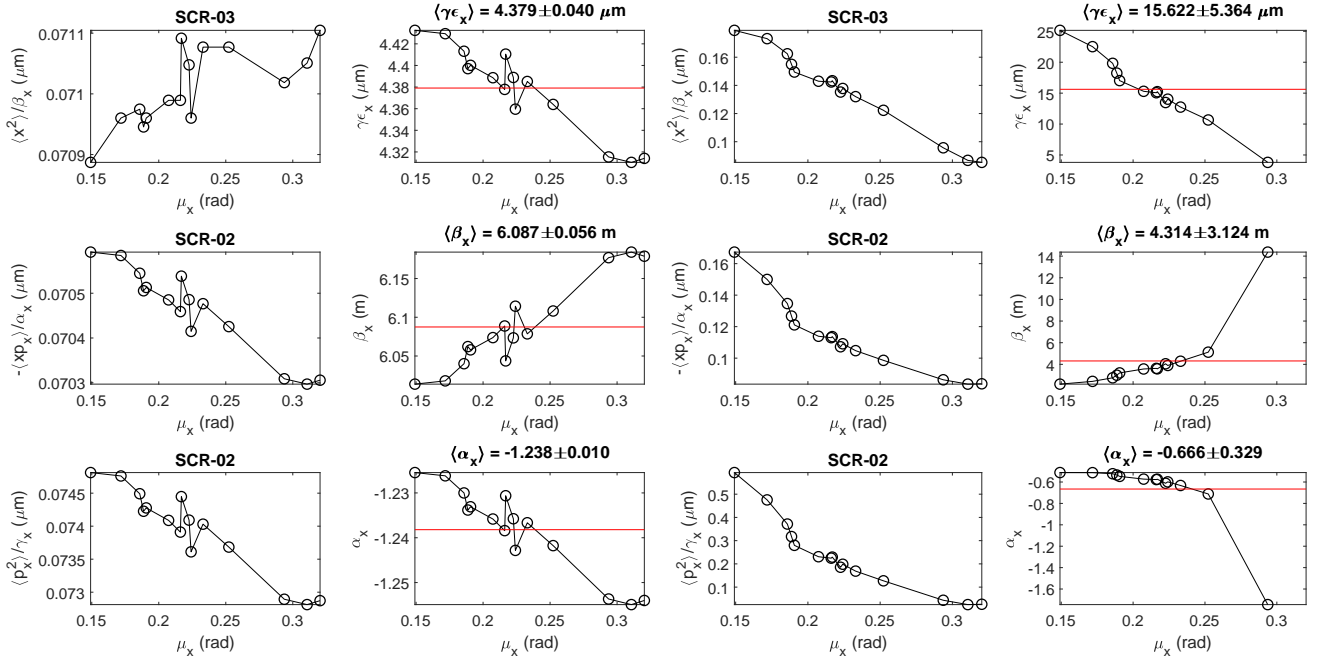


FIG. 3: Comparison of simulation results for the three-screen optics measurement method using different phase space distributions, for the transverse horizontal motion. The plots in the first and third columns show, for Gaussian and realistic phase space distributions respectively, the scaled covariance matrix elements $\langle x^2 \rangle / \beta_x$ at SCR-03 (top), $-\langle xp_x \rangle / \alpha_x$ at SCR-02 (middle), and $\langle p_x^2 \rangle / \gamma_x$ at SCR-02 (bottom). The plots in the second and fourth columns show, again for the Gaussian and realistic phase space distributions respectively, the normalised emittance (top), beta function (middle) and alpha function (bottom). Note the differences in vertical scales for the sets of plots for the Gaussian and the realistic phase space distributions. In the Gaussian case, there is only a very small variation in the quantities shown, as a function of the quadrupole strengths (used to vary the horizontal phase advance, given on the horizontal axis on each plot). The Gaussian distribution was constructed with nominal parameter values $\gamma \epsilon_x = 4.1 \mu\text{m}$, $\beta_x = 6.49 \text{ m}$ and $\alpha_x = -1.32$ at SCR-02. The case of the realistic phase space distribution shows very much larger variation in the calculated covariance matrix, emittance and optical functions, and displays some similarities with the experimental case (Fig. 2).

B. Quadrupole scan method

One of the limitations of the three-screen analysis method described in Section III A is the inability to provide information on beam coupling. This can be overcome, however, by combining observations of the transverse beam size at different screens for various strengths of the quadrupoles between the screens. If a sufficient number of quadrupole strengths are used, then beam size measurements at a single screen provide sufficient data to calculate the 4×4 transverse beam covariance matrix at a point upstream of the quadrupoles. The 4×4 covariance matrix has ten independent elements: in principle, just four sets of quadrupole strengths provide twelve beam size measurements (values for $\langle x^2 \rangle$, $\langle y^2 \rangle$ and $\langle xy \rangle$ for each set of quadrupole strengths), and are more than sufficient to determine the covariance matrix. In practice, it is desirable to use a greater number of quadrupole strength settings, to over-constrain the covariance matrix.

The quadrupole scan technique that we use is similar to that presented by Prat and Aiba [23]. The theory can be developed as follows. The covariance matrix Σ_3

at a location s_3 in the beamline (SCR-03 in the case of CLARA FE) is related to the covariance matrix Σ_2 at a location s_2 (SCR-02 in CLARA FE) through Eq. (19), where all matrices are now 4×4 . The relationship between the observable quantities at s_3 (assuming a YAG screen at that location) and the independent elements of Σ_2 can be written:

$$\begin{pmatrix} \langle x_3^2 \rangle_{(1)} \\ \langle x_3 y_3 \rangle_{(1)} \\ \langle y_3^2 \rangle_{(1)} \\ \langle x_3^2 \rangle_{(2)} \\ \langle x_3 y_3 \rangle_{(2)} \\ \langle y_3^2 \rangle_{(2)} \\ \langle x_3^2 \rangle_{(3)} \\ \langle x_3 y_3 \rangle_{(3)} \\ \langle y_3^2 \rangle_{(3)} \\ \vdots \end{pmatrix} = D \begin{pmatrix} \langle x_2^2 \rangle \\ \langle x_2 p_{x2} \rangle \\ \langle x_2 y_2 \rangle \\ \langle x_2 p_{y2} \rangle \\ \langle p_{x2}^2 \rangle \\ \langle p_{x2} y_2 \rangle \\ \langle p_{x2} p_{y2} \rangle \\ \langle y_2^2 \rangle \\ \langle y_2 p_{y2} \rangle \\ \langle p_{y2}^2 \rangle \end{pmatrix}, \quad (23)$$

where $\langle x_3^2 \rangle_{(n)}$ represents the mean square horizontal transverse beam size measured at s_3 for a particular set of quadrupole strengths, and similarly for $\langle y_3^2 \rangle_{(n)}$ and $\langle x_3 y_3 \rangle_{(n)}$. With measurements of the beam distribu-

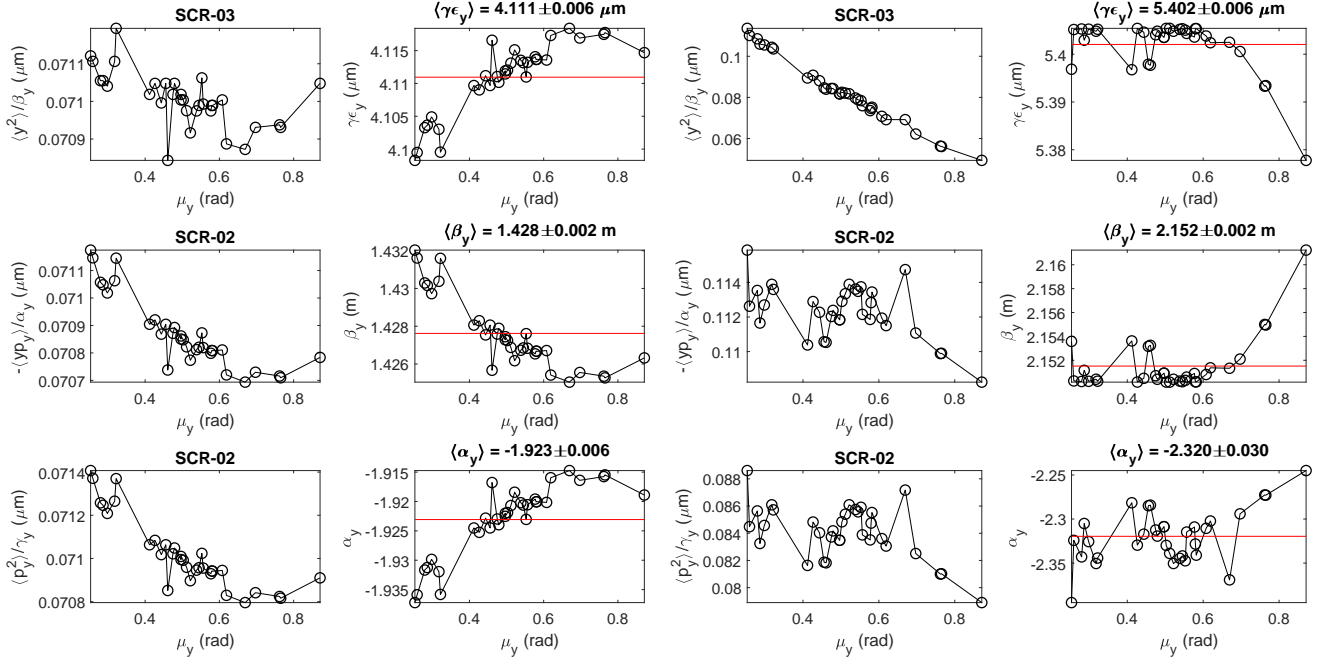


FIG. 4: Comparison of simulation results for the three-screen optics measurement method using different phase space distributions, for the vertical motion. The plots in the first and third columns show, for Gaussian and realistic phase space distributions respectively, the scaled covariance matrix elements $\langle y^2 \rangle / \beta_y$ at SCR-03 (top), $-\langle yp_y \rangle / \alpha_y$ at SCR-02 (middle), and $\langle p_y^2 \rangle / \gamma_y$ at SCR-02 (bottom). The plots in the second and fourth columns show, again for the Gaussian and realistic phase space distributions respectively, the normalised emittance (top), beta function (middle) and alpha function (bottom). Note the differences in vertical scales for the sets of plots for the Gaussian and the realistic phase space distributions. In the Gaussian case, there is only a very small variation in the quantities shown, as a function of the quadrupole strengths (used to vary the vertical phase advance, given on the horizontal axis on each plot). The Gaussian distribution was constructed with nominal parameter values $\gamma_{\epsilon_y} = 4.1 \mu\text{m}$, $\beta_y = 1.43 \text{m}$ and $\alpha_y = -1.92$ at SCR-02. The case of the realistic phase space distribution shows very much larger variation in the calculated covariance matrix, emittance and optical functions, and displays some similarities with the experimental case (Fig. 2).

tion in co-ordinate space at s_3 for N different sets of quadrupole strengths, D is a $3N \times 10$ matrix. The elements of D can be found, using Eq. (19), from the transfer matrices M_{23} from s_2 to s_3 (with each set of three

rows in D corresponding to a single set of quadrupole strengths). Explicit expressions for the elements of D (for a given transfer matrix) are as follows:

$$D^T = \begin{pmatrix} m_{1,1}^2 & m_{1,1}m_{3,1} & m_{3,1}^2 \\ 2m_{1,1}m_{1,2} & m_{1,2}m_{3,1} + m_{1,1}m_{3,2} & 2m_{3,1}m_{3,2} \\ 2m_{1,1}m_{1,3} & m_{1,3}m_{3,1} + m_{1,1}m_{3,3} & 2m_{3,1}m_{3,3} \\ 2m_{1,1}m_{1,4} & m_{1,4}m_{3,1} + m_{1,1}m_{3,4} & 2m_{3,1}m_{3,4} \\ m_{1,2}^2 & m_{1,2}m_{3,2} & m_{3,2}^2 \\ 2m_{1,2}m_{1,3} & m_{1,3}m_{3,2} + m_{1,2}m_{3,3} & 2m_{3,2}m_{3,3} \\ 2m_{1,2}m_{1,4} & m_{1,4}m_{3,2} + m_{1,2}m_{3,4} & 2m_{3,2}m_{3,4} \\ m_{1,3}^2 & m_{1,3}m_{3,3} & m_{3,3}^2 \\ 2m_{1,3}m_{1,4} & m_{1,4}m_{3,3} + m_{1,3}m_{3,4} & 2m_{3,3}m_{3,4} \\ m_{1,4}^2 & m_{1,4}m_{3,4} & m_{3,4}^2 \end{pmatrix}, \quad (24)$$

where $m_{i,j}$ is the (i,j) element of the transfer matrix M_{23} (for a given set of quadrupole strengths). Given observa-

tions of the beam profile at s_3 for a number of different sets of quadrupole strengths, and the corresponding val-

ues for the elements of D , the elements of the covariance matrix at s_2 may be found by inverting Eq. (23). Since D is not a square matrix, the pseudo-inverse of D (found, for example, using singular value decomposition) must be used instead of the strict inverse.

It is worth noting that whereas in one degree of freedom it is possible to obtain the elements of the covariance matrix at the Reconstruction Point by varying the strength of a single quadrupole between the Reconstruction Point and the Observation Point, this is not the case in two degrees of freedom. To understand the reason for this, consider the case of a single thin quadrupole with the Reconstruction Point s_2 at the upstream (entrance) face of the quadrupole, and the Observation Point s_3 some distance downstream from the quadrupole. The elements of the covariance matrix $\langle x_3^2 \rangle$, $\langle x_3 y_3 \rangle$ and $\langle y_3^2 \rangle$ each have a quadratic dependence on the quadrupole strength, with coefficients determined by the elements of the covariance matrix at the Reconstruction Point. By fitting the quadratic curves obtained from a quadrupole scan we therefore obtain nine constraints (three for each of the observed elements of the covariance matrix at s_2); however, the covariance matrix at s_2 has ten independent elements (in two degrees of freedom). The problem is therefore underconstrained: in the context of Eq. (23) this is manifest as the matrix D having fewer non-zero singular values than are required to determine uniquely the elements of the covariance matrix at the Observation Point. Although it is always possible to “invert” D using singular value decomposition, the procedure in this case would yield a solution for the covariance matrix that minimises the sum of the squares of the matrix elements: there is no reason to suppose that this least-squares matrix is near the correct solution. To address this problem, however, it is only necessary to collect data from a scan of two quadrupoles at different locations between the Observation Point and the Reconstruction Point. This breaks the degeneracy in the system, and (if the system is properly designed) more than ten singular values of D will be non-zero: in other words, the system becomes overconstrained, rather than under-constrained.

The same data collected for the three-screen method can be used in the analysis using the quadrupole scan method, and the same practical considerations (concerning, for example, the desirability of a beam waist at the Reconstruction Point, and maintaining an approximately round beam at the Observation Point) apply. However, it should be noted that for the three-screen method, the observed beam sizes at all three screens are used to reconstruct the covariance matrix: an independent reconstruction is obtained for each point in the quadrupole scan. For the quadrupole scan analysis method, on the other hand, we use only the observed beam size at a single screen (SCR-03 in this case) and combine all the measurements for different quadrupole strengths to calculate the elements of the covariance matrix. In effect, we calculate the size and shape of the distribution in phase space based on the widths of projections at many differ-

ent phase angles: this leads to a more reliable result than is obtained using the three-screen analysis method, for which only three different phase angles are used. Nevertheless, even for a large number of phase angles, the quadrupole scan method does not provide the same detailed information on the phase space distribution that is provided by the tomography method (discussed in Section III C). Rather, it fits a phase space distribution that may have significant detailed structure with a simple Gaussian distribution.

Figure 5 shows the residuals from a fit based on data from a quadrupole scan in CLARA FE made with nominal machine settings. Each point indicates the observed and fitted beam size ($\langle x^2 \rangle$, $\langle y^2 \rangle$ or $\langle xy \rangle$) at the Observation Point for a different set of strengths of the quadrupoles between SCR-02 (the Reconstruction Point) and SCR-03 (the Observation Point). The results may also be validated by comparing the beam size predicted at the Reconstruction Point with the actual beam size observed at this point. For the case shown, the agreement is within about 15%.

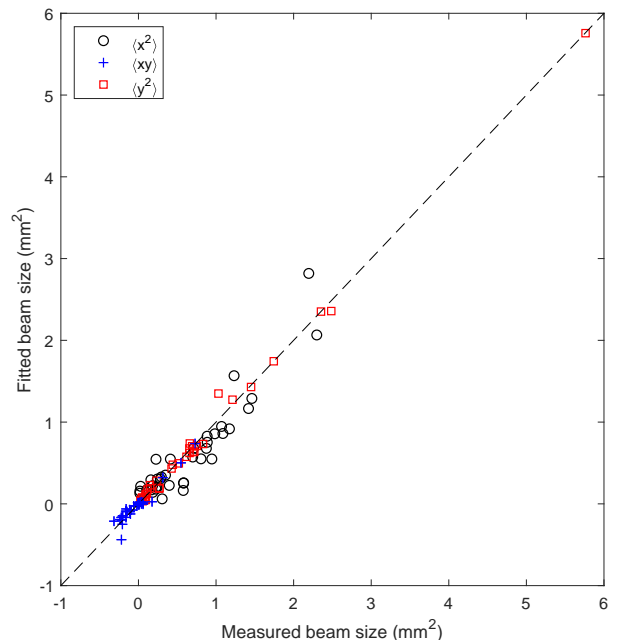


FIG. 5: Beam size at SCR-03 reconstructed from a quadrupole scan analysis compared with the beam size observed directly on the screen. Each point corresponds to a different set of quadrupole strengths. Circles indicate the horizontal beam size $\langle x^2 \rangle$; boxes indicate the vertical beam size $\langle y^2 \rangle$; crosses indicate the horizontal-vertical correlation $\langle xy \rangle$. The distances of the points from the dashed line (which passes through the origin with unit gradient) indicates the residuals to the fit.

C. Phase space tomography

Finally, it is possible to use phase space tomography to construct a more detailed representation of the beam properties than is provided by just the emittance and optical functions. In principle, the tomography method is similar to the quadrupole scan, in that by observing the beam image on a screen for different strengths of a set of upstream quadrupoles, it is possible to reconstruct the phase space distribution at a point upstream of the quadrupoles. The difference is that for the quadrupole scan, only the rms beam sizes are used in the analysis: tomography uses all the information from the (observed) beam distribution to produce a more detailed reconstruction of the phase space distribution of the beam. When tomography is carried out in co-ordinate space, two-dimensional images (projections) on a screen for different orientations of an object are used to reconstruct a three-dimensional representation of the object. In phase space tomography, different ‘‘orientations’’ correspond to rotations in phase space, which are achieved by changing the horizontal or vertical phase advances between the Reconstruction Point and the Observation Point. Mathematically, the analysis is essentially the same as in co-ordinate space, and standard algorithms developed for tomography in co-ordinate space (such as filtered back-projection, or maximum entropy [25–27]) can be applied to phase space tomography.

For analysis of data from CLARA FE, we have used a form of algebraic reconstruction. The procedure may be outlined as follows. For simplicity we consider just a single degree of freedom: the generalisation to two (or more) degrees of freedom is straightforward. Let ψ be a vector in which each element ψ_j represents the beam density at a particular point (x_j, p_{xj}) in phase space at the Reconstruction Point. Assuming that the points are evenly distributed on a grid in phase space, then the projected beam density at the Observation Point, $\rho_i^{(1)}$ at a point $x = x_i$ in co-ordinate space, can be written as a matrix multiplication:

$$\rho_i^{(1)} = \sum_j P_{ij}^{(1)} \psi_j, \quad (25)$$

where the matrix $P^{(1)}$ has elements:

$$P_{ij}^{(1)} = \begin{cases} 1 & \text{if } x_i = m_{1,1}^{(1)} x_j + m_{1,2}^{(1)} p_{xj}, \\ 0 & \text{otherwise.} \end{cases} \quad (26)$$

$m_{1,1}^{(1)}$ and $m_{1,2}^{(1)}$ are elements of the transfer matrix from the Reconstruction Point to the Observation Point, for a given set of quadrupole strengths. If the vector ρ has \mathcal{N} elements ρ_i , and there are \mathcal{N}^2 points (x_j, p_{xj}) in phase space, then $P^{(1)}$ is an $\mathcal{N} \times \mathcal{N}^2$ matrix. If the transfer matrix from the Reconstruction Point to the Observation Point is changed (e.g. by changing the strengths of the quadrupoles between the two points), then we construct a new vector $\rho^{(2)}$ from the new image at the Observation Point, corresponding to the new transfer matrix. In

general, for the n th transfer matrix, we have:

$$\rho_i^{(n)} = \sum_j P_{ij}^{(n)} \psi_j. \quad (27)$$

Note that the phase space density ψ is constant, because ψ refers to a point upstream of any quadrupoles whose strength is changed during the measurements. We can combine the observations simply by stacking the vectors $\rho^{(n)}$ and the matrices $P^{(n)}$:

$$\rho = \begin{pmatrix} \rho^{(1)} \\ \rho^{(2)} \\ \vdots \\ \rho^{(n)} \end{pmatrix}, \quad \text{and} \quad P_{ij} = \begin{pmatrix} P^{(1)} \\ P^{(2)} \\ \vdots \\ P^{(n)} \end{pmatrix}. \quad (28)$$

ρ is a vector with $n\mathcal{N}$ elements, and P is an $n\mathcal{N} \times \mathcal{N}^2$ matrix. In terms of the pseudo-inverse P^\dagger of P , we have the following formula for the phase space density at the Reconstruction Point:

$$\psi_j = \sum_i P_{ji}^\dagger \rho_i. \quad (29)$$

We perform the analysis in normalised phase space [16], in which the phase space variables (x_N, p_{xN}) are defined by:

$$\begin{pmatrix} x_N \\ p_{xN} \end{pmatrix} = \begin{pmatrix} \frac{1}{\sqrt{\beta_x}} & 0 \\ \frac{\alpha_x}{\sqrt{\beta_x}} & \sqrt{\beta_x} \end{pmatrix} \begin{pmatrix} x \\ p_x \end{pmatrix}, \quad (30)$$

where α_x and β_x are the Courant–Snyder functions at the given point in the beam line. The transfer matrix in normalised phase space between any two points in the beam line is represented by a pure rotation matrix, with rotation angle given by the phase advance. This simplifies the implementation of the algebraic tomography method described above. A further advantage of working in normalised phase space is that if the Courant–Snyder functions at the Reconstruction Point are chosen to match the beam distribution, then the beam distribution in phase space at this point will be perfectly circular: this improves the accuracy with which parameters such as the emittance may be calculated. Note that, since we do not know in advance the actual Courant–Snyder parameters describing the beam distribution at the Reconstruction Point, we need to make some estimate based on (for example) simulations or a quadrupole scan analysis. In practice, it is not essential for the estimated parameters to match exactly the actual beam parameters: any discrepancy will simply lead to an elliptical distortion of the beam distribution in normalised phase space. To work in normalised phase space is straightforward: all that is necessary is to scale the co-ordinate axis for the observed beam projection by a factor $1/\sqrt{\beta_x^{\text{OP}}}$, where β_x^{OP} is the Courant–Snyder beta function at the Observation Point calculated from the estimated (fixed) Courant–Snyder functions at the Reconstruction Point

and the transfer matrix from the Reconstruction Point to the Observation Point.

Rather than compute the pseudo-inverse of P , we solve Eq. (27) iteratively, using a least-squares method. For the computation of the phase space in a single degree of freedom, we apply a constraint that the particle density must be positive at all points in phase space. However, applying this constraint carries considerable computation overhead, and for computation of the phase space in two degrees of freedom, which has considerably greater computational cost than the case of a single degree of freedom, we do not constrain the least-squares solver in this way. This can result in negative (unphysical) values for the particle density at some points in phase space; however, when a good fit is achieved, the negative values make a relatively small contribution to the overall phase space distribution.

Although there is no need for the phase advances between the Reconstruction Point and Observation Point to be evenly distributed over the set of observations for different quadrupole strengths, it generally improves the accuracy of the tomography analysis to use as wide a range of phase advances as possible, with roughly uniform spacing: this maximises the overall constraints on the phase space distribution for a given number of observations. The sets of quadrupole strengths identified in the preparatory simulations (described above) were chosen to provide a wide range of phase advances. The same data (screen images at the Observation Point, for a range of different quadrupole strengths) can be used for the three-screen analysis (described in Section III A), the quadrupole scan analysis (described in Section III B) and the tomography analysis described here. Figure 6 shows a set of results from tomography analysis for the nominal machine settings, and in which the horizontal and vertical phase spaces are treated independently. As was the case for the quadrupole scan method, the results may be validated by comparing the predicted beam size at the Reconstruction Point with the beam observed directly at this point (SCR-02): the results of the comparison are shown in the lower plots in Fig. 6. There is good agreement, and it can be clearly seen that the tomography analysis reveals some features of the charge distribution in phase space that are not obtained from the quadrupole scan analysis.

Treating the horizontal and vertical phase spaces separately in the analysis means that no information is provided on coupling in the beam, which may arise (for example) from incorrect setting of the bucking coil at the electron source. It is possible to extend the tomography analysis from a single degree of freedom, to treating two degrees of freedom simultaneously [14]. Applying this technique to the case considered here, the resulting four-dimensional phase space reconstruction includes information about the betatron coupling in the beam. Some results from experimental data (screen images) are shown in Fig. 8(a). Generally, the fit using Eq. (29) of the phase space beam density to the observed images is very

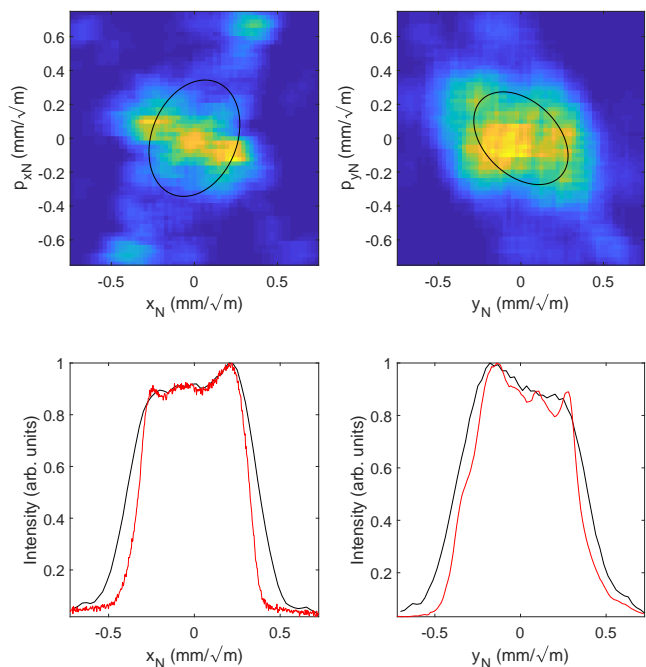


FIG. 6: Results from phase space tomography in CLARA FE, treating horizontal and vertical phase spaces separately. The top plots show the charge density in the beam at SCR-02 in the horizontal (left) and vertical (right) phase spaces, in normalised variables (co-ordinates scaled by the square root of the beta function). The black ellipses show the emittance ellipses fitted to the phase space distribution, so as to satisfy (6). The bottom plots show the density projected onto the horizontal (left) or vertical (right) axes: black lines are from the tomographic reconstruction, red lines are from direct observation of the beam image on SCR-02.

good: the residuals from a typical example are shown in Fig. 7.

One drawback of applying phase space tomography in two degrees of freedom is that the matrix P in Eq. (25) becomes very large: in one degree of freedom, to reconstruct the phase space distribution with resolution \mathcal{N} in each dimension using n observations, P will be an $n\mathcal{N} \times \mathcal{N}^2$ matrix. In two degrees of freedom (four-dimensional phase space), P will be an $n\mathcal{N}^2 \times \mathcal{N}^4$ matrix: even for a relatively coarse reconstruction, with \mathcal{N} of order 50, computing P and applying its inverse can require significant computational resources. The situation is eased somewhat by the fact that in practice, P is a sparse matrix, and this allows a significant reduction in the computer memory that would otherwise be required; nevertheless, the required computational resources can be a limit on the resolution with which the phase space in two degrees of freedom may be reconstructed. The results shown here use a four-dimensional phase space resolution $\mathcal{N} = 69$.

Projections from the four-dimensional phase space density found from experimental data in CLARA FE are

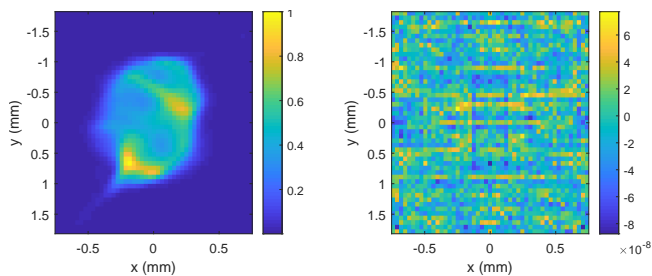


FIG. 7: Left: typical beam image at SCR-03 (the Observation Point) for one point in a quadrupole scan. The image reconstructed from the four-dimensional phase space density found using Eq. (29) extended to two degrees of freedom (projecting the phase space density ψ into co-ordinate space) is visually indistinguishable from the observed image. Right: residuals of the fit, representing the difference between the intensity of each pixel in the observed image, and the intensity of the corresponding pixel in the image reconstructed from the four-dimensional phase space density. The beam image (left) is scaled so that the intensity varies between 0 (dark blue) and 1 (yellow); on this scale, the largest residuals (right) are of order 10^{-7} .

shown in Fig. 8 (a). To validate the technique, we take the four-dimensional phase space distribution, and use it in a simulation to construct a set of images on SCR-03 corresponding to different quadrupole strengths. We then take the simulated images, and again apply the tomography analysis: the results are shown in Fig. 8 (b). Although there are some differences between the original and reconstructed distributions they are sufficiently close to indicate that the technique potentially has good accuracy. We also find that there is good agreement between the emittances and optics functions obtained by fitting ellipses to the projections of the phase space into the horizontal and vertical planes (see Table I).

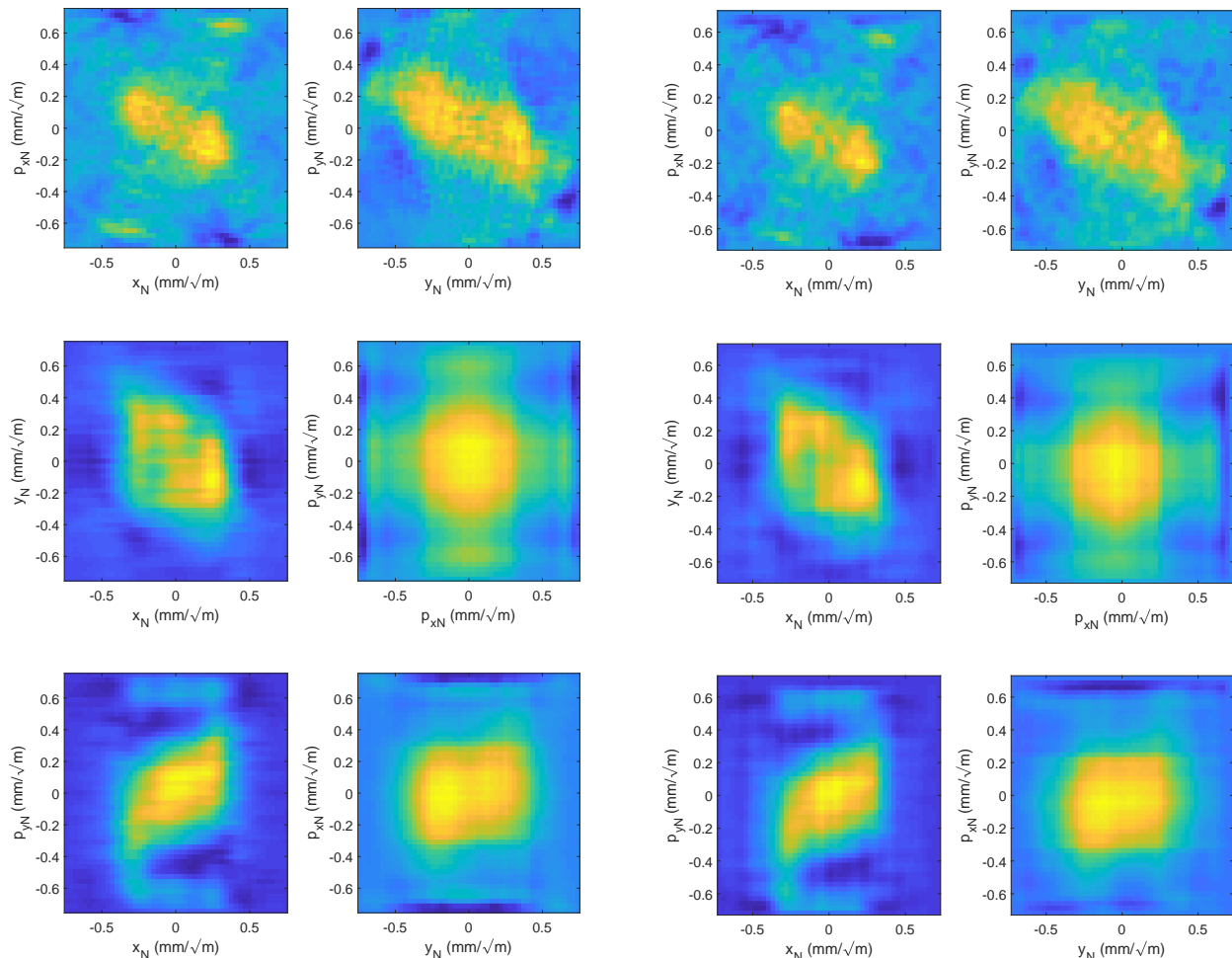
We can further validate the results by reconstructing the two-dimensional distribution in co-ordinate space at the Reconstruction Point (by projecting the four-dimensional phase space distribution onto the co-ordinate axes), and comparing this with the image that is observed directly. Some examples for such comparisons are shown in Fig. 9. In general, we find that the images reconstructed from phase space tomography reproduce reasonably well the general shape and some of the more detailed features of the images that are observed directly. However, the tomography does not reveal the same level of detail as can be seen in the observed image. This may be due in part to the limited resolution of the tomography analysis: for the analysis presented here, we used a phase space resolution of 69 points on each of the four axes (which was at the upper limit set by the available computer memory). However, it is also likely that measurement errors also play a role. We note that the residuals of the fits to the images at the Observation Point are typically very small (so that there is no discernible difference between the directly-observed images at this point

and the images reconstructed from phase space tomography: see the example in Fig. 7). However, there are systematic differences between the reconstructed images at SCR-02 (the Reconstruction Point), and the images observed directly on that screen. In particular, the vertical size of the reconstructed beam (projecting the phase space distribution onto the vertical axis) is generally of order 10% larger than the vertical size of the image observed directly. Work is in progress to understand and correct the systematic errors: possible sources include calibration errors in the quadrupoles and in the diagnostics used for collecting beam images. It is important to have accurate values for the quadrupole strengths, since the tomographic analysis depends on knowing the betatron phase advance between the Reconstruction Point and the Observation Point, as well as the optical functions at the Observation Point for given values of these functions at the Reconstruction Point. Similarly, the analysis depends on accurate knowledge of the calibration factors of the diagnostic screens. Hysteresis in the quadrupole magnets used to change the optics between the Reconstruction Point and the Observation Point may also lead to errors in the analysis: to try to minimise hysteresis effects, the quadrupoles were routinely degaussed (cycled) between scans, but the time taken for this procedure made it impractical to degauss the quadrupoles at each point in a single scan.

IV. EMITTANCE AND OPTICS MEASUREMENTS UNDER VARIOUS MACHINE CONDITIONS

A. Nominal machine settings

Table I shows the emittance and optics parameters obtained under nominal machine settings using the three different techniques discussed in the previous sections: three-screen measurements, quadrupole scans, and phase space tomography. With the nominal machine settings, the electron source and linac operate with the beam on-crest of the rf (i.e. to give maximum beam acceleration for a given rf amplitude), with amplitudes producing beam momentum 5 MeV/c and 30 MeV/c respectively. The current in the bucking coil is set to cancel the solenoid field on the photocathode, and the laser intensity is set to give a bunch charge of 10 pC. The results in Table I are based on the same data set (i.e. the same set of beam images) in each case; the only difference between the different methods is in the way that the data are analysed. In principle, therefore, we expect to see good agreement between the values obtained using different techniques. The quadrupole scan and tomography techniques do indeed produce values in broad agreement. In the case of the three-screen analysis, however, the values found are significantly different from those obtained using the other techniques. As discussed in Section III A, this is probably because of the complicated structure of the beam in phase



(a) Phase-space distribution from tomography analysis of experimental data.

(b) Phase-space distribution from tomography analysis of simulated data.

FIG. 8: Projections of beam density in normalised phase space, found from phase space tomography in two degrees of freedom in CLARA FE. Each plot shows a different projection of the charge density from four-dimensional phase space, using normalised phase space variables. Coupling in the beam is evident in the tilt of the charge distribution in the cases that the axes refer to different degrees of freedom. The left-hand set of plots (a) shows the phase space distribution reconstructed from experimental data; the right-hand set of plots (b) shows the results of the tomography analysis applied to simulated data based on the measured phase space distribution, to validate the technique. Although there are some differences between the analysis results from the experimental data and the results from the simulated data, there is overall very good agreement in the phase space distribution found in each case, and in the emittances and optical functions corresponding to fitted emittance ellipses (see Table I).

space. Under such conditions, the quadrupole scan and tomography methods produce more reliable (and meaningful) results.

For the quadrupole scan and tomography analysis in four-dimensional phase space, the emittance and optics values given are those for the normal mode quantities as described in Section II. The close agreement with the uncoupled values (two-dimensional phase space) indicates that coupling is small in this case (as expected from the machine settings). The emittance and optics values in

the case of the tomography analysis are determined from the covariance matrix with elements calculated by averaging over the phase space density.

B. Effect of varying bucking coil strength

The electron source in CLARA FE is constructed so that the field from the solenoid can be cancelled at the cathode by the field from a bucking coil. If the current

TABLE I: Comparison of values for normalised emittances and Courant–Snyder parameters determined from different analysis techniques. The results from analysis in four-dimensional phase space are for the normal mode emittances and coupled optical functions (see Section II). The values for the three-screen analysis technique show the mean and standard deviation of the results of the analysis over each point in the quadrupole scan, omitting points that do not return a real value for the emittance. The three-screen analysis method neglects any detailed structure in the beam distribution in phase space, and in this case leads to unreliable results.

	Two-dimensional phase space			Four-dimensional phase space			
	Three-screen	Quad scan	Tomography		Quad scan	Tomography measurement	Tomography simulation
$\epsilon_{N,x}$ (μm)	39.7 ± 6.7	11.3	5.31	$\epsilon_{N,I}$ (μm)	7.49	4.96	4.78
β_x (m)	1.92 ± 0.62	6.57	16.4	β_{11}^I (m)	8.84	19.8	20.8
α_x	-0.231 ± 0.060	-1.37	-1.64	$-\beta_{12}^I$	-1.51	-2.03	-2.30
$\epsilon_{N,y}$ (μm)	4.86 ± 0.11	4.80	4.20	$\epsilon_{N,II}$ (μm)	3.47	2.61	2.52
β_y (m)	1.25 ± 0.03	1.26	1.61	β_{33}^{II} (m)	1.79	1.29	1.30
α_y	-1.53 ± 0.21	-1.80	-1.75	$-\beta_{34}^{II}$	-1.82	-1.29	-1.29

in the bucking coil is changed from the value needed to achieve cancellation, electrons are emitted from the surface of the cathode in a non-zero solenoid field: the effect is to introduce some coupling into the beam (as a result of non-compensated azimuthal momentum), which can appear as changes in the beam emittances. In particular, the individual normal mode emittances will vary, though their product should remain constant as a function of the solenoid field strength on the cathode [28, 29]. The difference between the normal mode emittances is expected to be minimised when there is zero solenoid field on the cathode: with increasing field strength (parallel to the longitudinal axis, in either direction) one emittance will increase while the other will decrease. Tuning the machine for optimum performance generally involves minimising the coupling, to achieve the smallest possible emittance ratio [15], and characterising and understanding the coupling as a function of the strength of the bucking coil is thus an important step in machine commissioning. Four-dimensional phase space tomography offers a powerful tool for providing insight into coupling in the machine, and was used to study the dependence of the phase space distribution on the strength of the bucking coil.

The normal mode emittances as a function of current in the bucking coil, found from four-dimensional phase space tomography (as described in Section III B) are shown in Fig. 10. Although there is some variation in the product of the emittances with changes in the current in the bucking coil, over a wide range the variation is small. There is also some indication of the expected behaviour of the individual emittances. The difference between the emittances is minimised for a bucking coil current of approximately -1.5 A: this is somewhat different from the nominal value of -2.2 A for cancelling the field on the cathode. The reason for the discrepancy is being investigated. Note that before collecting data over the range of bucking coil currents, the bucking coil was degaussed with the intention of improving the agreement between the cathode field calculated from a computer model of the electron source and the field that was actually pro-

duced for a given current. It is also worth noting that the time taken for data collection over the full range of bucking coil currents took several hours, and it is likely that some variation in machine parameters (such as rf phase and amplitude in the electron source and linac) occurred over this time.

Also shown in Fig. 10 are results from a GPT simulation and from a simple theoretical model: these are included in the figure to illustrate the expected behaviour of the normal mode emittances as a function of the solenoid field on the cathode, and are not intended to show results from an accurate machine model. For the simulations, we use parameters for the electron source corresponding to those in CLARA FE, but with the field from the bucking coil scaled to cancel the solenoid field on the cathode for a current of -1.5 A in the the bucking coil (rather than the nominal -2.2 A). Also, the initial distribution of particles in phase space is chosen to give emittances (with zero solenoid field on the cathode) corresponding to the experimental measurements. This requires values for the beam size and divergence at the cathode that are significantly different from the values believed to be appropriate for CLARA FE, by a factor of two in spot size, and up to an order of magnitude in divergence; however, it should be remembered that in the simulation, the emittances are calculated immediately after the electron source, whereas the measurements are made in a section of beamline downstream of the linac and numerous other components. Effects (that are not yet well characterised) between the electron source and the measurement section are likely to lead to some increase in emittance. The GPT and theoretical results are therefore included in Fig. 10 purely to illustrate the expected behaviour of the emittances as functions of the strength of the solenoid field on the cathode, rather than as a direct comparison of an accurate computational model with the experimental results.

Also shown in Fig. 10 are results from a simplified theoretical (analytical) model. This is based on an assumed beam phase space distribution at the cathode, i.e. immediately after photoemission. If there is no magnetic field

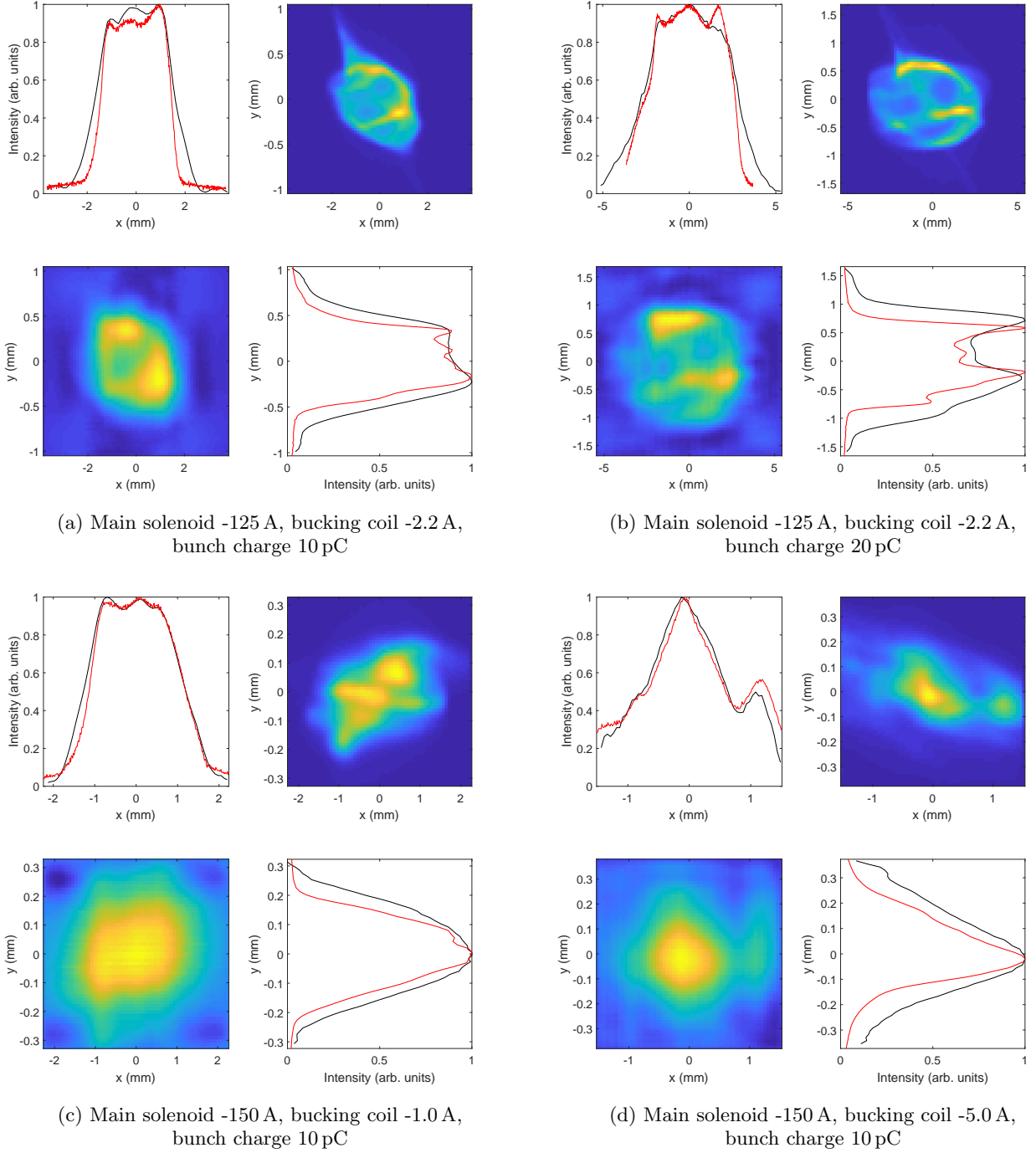


FIG. 9: Comparison between beam images observed directly at SCR-02 and the reconstruction of the images from phase space tomography in two degrees of freedom for a range of solenoid and bucking coil currents in the electron source and different bunch charges in CLARA FE. Within each subfigure, the plot at the top right shows the beam image observed directly on SCR-02; the plot at bottom left shows the charge distribution in co-ordinate space reconstructed from phase space tomography (a projection of the four-dimensional phase space onto the co-ordinate plane) at the same location. The plots at top left and bottom right in each subfigure show the charge density projected onto the horizontal and vertical axes, respectively: black lines are from the tomography analysis and red lines are from the directly observed image.

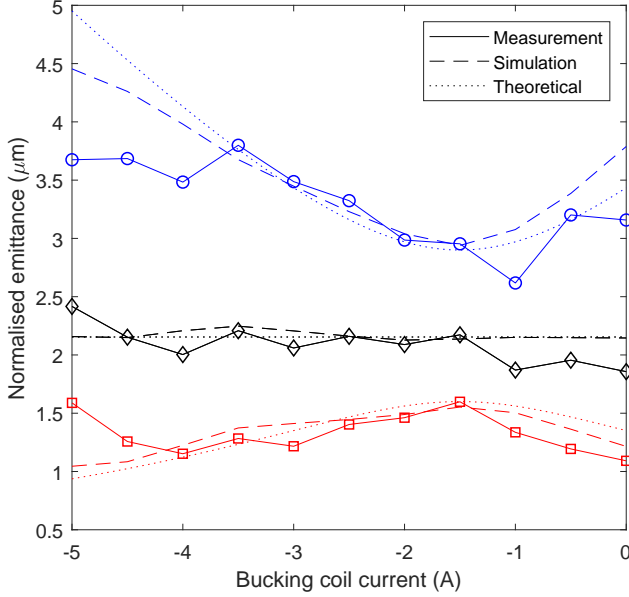


FIG. 10: Normalised normal mode emittances as a function of current in the bucking coil at the electron source, with fixed bunch charge and main solenoid current. The solid lines show experimental (measured) values determined from four-dimensional phase space tomography (as described in Section III C), the dashed lines show values from GPT simulations, and the dotted lines show values from a simple theoretical model. The upper and lower sets of lines (blue and red, respectively) show the normalised normal mode emittances; the middle set of lines (black) show the geometric mean of the emittances. Parameters in the simulations and theoretical model are chosen to fit the experimental results.

on the cathode, then the covariance matrix is characterised by an emittance and beta function in each transverse direction:

$$\Sigma = \begin{pmatrix} \beta_x \epsilon_x & 0 & 0 & 0 \\ 0 & \frac{\epsilon_x}{\beta_x} & 0 & 0 \\ 0 & 0 & \beta_y \epsilon_y & 0 \\ 0 & 0 & 0 & \frac{\epsilon_y}{\beta_y} \end{pmatrix}. \quad (31)$$

A solenoid field of strength B_0 on the cathode can be represented by a vector potential:

$$\mathbf{A} = \left(-\frac{1}{2}B_0y, \frac{1}{2}B_0x, 0 \right), \quad (32)$$

so that the canonical conjugate momenta p_x and p_y become:

$$p_x = \frac{\gamma m v_x + \frac{1}{2}eB_0y}{P_0}, \quad (33)$$

$$p_y = \frac{\gamma m v_y - \frac{1}{2}eB_0x}{P_0}, \quad (34)$$

where m and e are the mass and magnitude of the charge of the electron, v_x and v_y are the transverse

horizontal and vertical components of the velocity, and $P_0 = \beta_0 \gamma_0 m c$ is the reference momentum (which can be chosen arbitrarily). The covariance matrix then becomes:

$$\Sigma = \begin{pmatrix} \beta_x \epsilon_x & 0 & 0 & \eta \beta_x \epsilon_x \\ 0 & \frac{\epsilon_x}{\beta_x} + \eta^2 \beta_y \epsilon_y & -\eta \beta_y \epsilon_y & 0 \\ 0 & -\eta \beta_y \epsilon_y & \beta_y \epsilon_y & 0 \\ \eta \beta_x \epsilon_x & 0 & 0 & \frac{\epsilon_y}{\beta_y} + \eta^2 \beta_x \epsilon_x \end{pmatrix}, \quad (35)$$

where:

$$\eta = \frac{eB_0}{2P_0}. \quad (36)$$

Finally, from the covariance matrix (35), we find (using the methods described in Section II) that the normal mode emittances are given by:

$$\epsilon_{I,II} = \sqrt{\chi \pm \sqrt{\chi^2 - \epsilon_x^2 \epsilon_y^2}}, \quad (37)$$

where:

$$\chi = \frac{\epsilon_x^2 + \epsilon_y^2}{2} + 2\eta^2 \beta_x \epsilon_x \beta_y \epsilon_y. \quad (38)$$

The normalised emittances ($\epsilon_{N,I} = \beta_0 \gamma_0 \epsilon_I$, and similarly for $\epsilon_{N,II}$) remain constant during acceleration of particles in the rf field of the electron source (and in the linac). To apply this model to CLARA FE, giving the results shown in Fig. 10, the initial beam size and divergence are chosen to fit the emittances at their closest approach: the values used are close to those used in the GPT simulation. We also assume that $\eta = 0$ for a bucking coil current of -1.5 A, and scale the dependence of η on the field in the bucking coil so as to match the experimental curves. However, we again emphasise that the results from the theoretical model and the GPT simulation are included only to give an illustration of the expected behaviour, and are not directly comparable with the experimental results.

Direct inspection of the phase space distribution provides a further indication of how the coupling changes with the current in the bucking coil. For example, Fig. 11 shows the projection onto the x - p_y plane of the four-dimensional phase space (reconstructed from the tomography measurements) for different values of the current in the bucking coil. The ‘‘tilt’’ on the distribution corresponds to a correlation between the horizontal coordinate and vertical momentum, and indicates the coupling: we see that this changes sign as the bucking coil current is varied from 0 A to -3.5 A. The tilt (and hence the coupling) vanishes for a current of around -1.5 A, which is consistent with the current required to minimise the difference between the normal mode emittances.

A more complete characterisation of the coupling is given in Fig. 12, which shows the elements of the covariance matrix at SCR-02 (the Reconstruction Point) as functions of current in the bucking coil. Coupling between motion in the horizontal and vertical directions is indicated by non-zero values of the elements in the 2×2

top-right block diagonal. All these elements vanish for bucking coil currents of around -1.5 A. We do not expect this to correspond exactly to the bucking coil current that minimises the separation between the normal mode emittances, since after leaving the cathode (in zero longitudinal magnetic field) the particles then pass through a section of main solenoid field, not cancelled by the bucking coil. The main solenoid field introduces some coupling in the beam, characterised by non-zero elements off the 2×2 block diagonals in the covariance matrix. However, tracking simulations in GPT suggest that in the case of CLARA FE, the coupling in the covariance matrix introduced by the part of the main solenoid not cancelled by the bucking coil is small: the coupling in the covariance matrix is minimised at a current within about 0.2 A of the current that gives the closest approach of the normal mode emittances (see Fig. 10).

C. Effects of varying main solenoid strength and bunch charge

Although space-charge effects in CLARA FE are negligible in the section of beamline where the emittance and optics measurements are made (with beam momentum around 30 MeV/c), space-charge forces can play a significant role in the electron source, depending on the bunch length and the total bunch charge. In the studies reported here, the photocathode laser was operated with pulse length of 2 ps: in this regime, space-charge effects are expected to be weak, even at the higher bunch charges (up to 250 pC) achievable in the machine. However, screen images suggested some significant variation in beam parameters even at lower bunch charges. It is planned in the future to use phase space tomography for rigorous studies of the impact of bunch charge (and other parameters) on beam properties; but so far, the limited time available for collecting quadrupole scan data, together with some variability in the machine conditions, has made it impractical to make detailed, systematic measurements. Nevertheless, to provide some information on beam behaviour, quadrupole scans were performed for bunch charges of 10 pC, 20 pC and 50 pC, and for a reduced main solenoid current of 125 A, as well as the nominal 150 A. Some of the results from analysis of these quadrupole scans using phase space tomography in two degrees of freedom are shown in Fig. 9, which compares the reconstructed beam image at SCR-02 with the image observed directly on this screen.

The images in Fig. 9 also indicate significant detailed structure in the beam distribution, depending on main solenoid current, bucking coil current and bunch charge. This is apparent both from the image observed directly at the Reconstruction Point, and from the phase space distribution constructed from four-dimensional tomography. In such cases, the phase space cannot accurately be characterised simply by the emittances and optical functions that describe the covariance matrix. Never-

theless, to allow some comparison, we calculate the normal mode emittances and optical functions, using the method described in Section II: the values of the normal mode emittances and selected optical functions are shown in Table II. Although there are indications of some patterns (for example, an increase in emittance with bunch charge) no firm conclusions can be drawn because machine conditions between different quadrupole scans were not accurately reproducible. Nevertheless, the measurements that have been made demonstrate the potential value of four-dimensional phase space tomography for developing an understanding of the beam physics in a machine such as CLARA FE, and for tuning the machine for optimum performance.

V. SUMMARY AND CONCLUSIONS

We have presented the first experimental results from four-dimensional phase space tomography in an accelerator. The beam emittance and optical properties obtained from phase space tomography have been compared with results obtained using more commonly employed techniques, such as three-screen analysis and quadrupole scans. The comparisons show that where there are detailed structures in the beam distribution in phase space (so that the distribution cannot be described, for example, by a simple Gaussian), three-screen and quadrupole scan analysis provide limited, and not always reliable, information. The difficulty in the case of a non-Gaussian beam distribution, is that a detailed description of the distribution cannot simply be given in terms of a small number of parameters (emittance and Courant-Snyder parameters). Phase space tomography overcomes this limitation by providing the beam density at a number of points in phase space.

Our results for the phase space tomography analysis and the comparisons with other methods are supported by simulation studies. The results of the tomography analysis have been validated by comparing (for example) the beam image at the entrance of the measurement section of the beamline (the Reconstruction Point) obtained from a projection of the measured four-dimensional phase space, with the beam image observed directly on a screen at this point. In general, the agreement suggests that four-dimensional phase space tomography is providing a useful representation of the beam properties, though the image reconstructed from tomography lacks the same resolution as the image observed directly. There is also evidence for systematic errors in the measurement that need to be properly understood.

A benefit of four-dimensional phase space tomography (compared to tomography in two-dimensional phase space) is that the technique provides detailed information on coupling in the beam. This can be important for tuning a machine such as CLARA FE, for example, where solenoids are used to provide focusing for the beam, but it is desirable to minimise the coupling that can be intro-

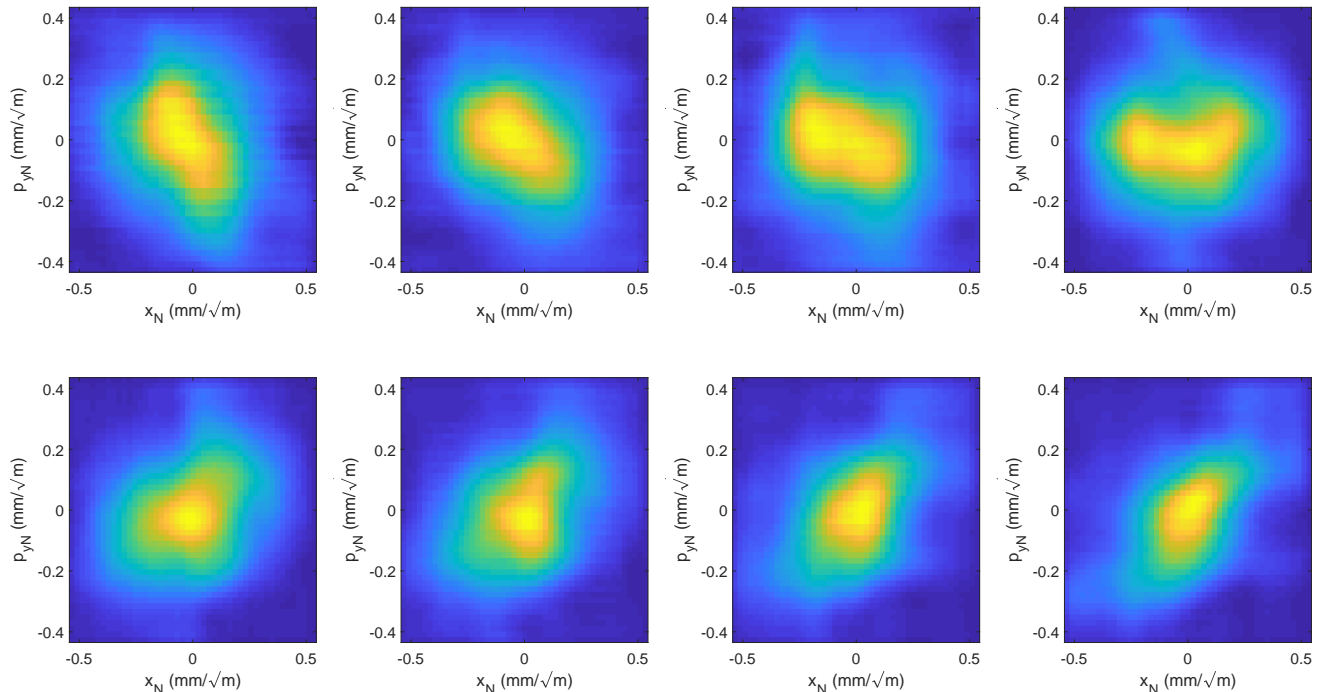


FIG. 11: Projection of the beam distribution in normalised phase space onto the x_N - p_{yN} plane, reconstructed from four-dimensional phase space tomography, showing variation of coupling with bucking coil current. From left to right, top to bottom, the bucking coil current increases from 0 A (top left) to -3.5 A (bottom right) in steps of -0.5 A. The correlation (tilt) between horizontal co-ordinate x_N and the vertical momentum p_{yN} indicates the strength of the coupling.

TABLE II: Beam emittances and optics parameters with different bunch charges and main solenoid strengths, with bucking coil current at the nominal -2.2 A. Note that measurements for some settings of the bunch charge and main solenoid strength were repeated (in particular: 10 pC bunch charge and -125 A main solenoid current; and 50 pC bunch charge and -150 A main solenoid current), to indicate the reproducibility of the tomography analysis for given machine settings.

Bunch charge (pC)	Main solenoid current (A)	$\epsilon_{N,I}$ (μm)	$\epsilon_{N,II}$ (μm)	β_{11}^I (m)	β_{33}^I (m)	β_{33}^I (m)	β_{11}^I (m)
10	-125	6.02	3.09	12.5	1.92	0.394	2.20
10	-125	10.2	6.33	11.8	1.45	0.368	3.39
10	-150	3.75	1.37	8.92	0.417	0.157	8.37
20	-125	13.7	5.93	15.8	3.52	0.287	3.97
20	-150	8.88	3.33	14.3	1.10	0.065	1.50
50	-150	8.98	4.47	18.8	0.981	0.121	3.28
50	-150	9.25	4.59	18.8	1.00	0.114	2.88

duced by those solenoids. Information on coupling can be obtained by applying the quadrupole scan method in two (transverse) degrees of freedom; but information obtained in this way may not be accurate or reliable if there is detailed structure in the beam distribution.

The main drawback of the tomography analysis is that collection of the data may be a time-consuming procedure. In cases where the beam distribution in phase space is smooth and without significant detailed structure (so that it can be well characterised by the emittance and optical functions) then the three-screen or quadrupole scan techniques, using a limited set of observations, may

provide sufficient information for machine tuning and optimisation relatively quickly. Phase space tomography generally requires data from a larger number of observations, but depending on the level of detail or accuracy required, it may be possible to minimise the number of points in the quadrupole scan used to provide the data: the limits of the technique have still to be rigorously explored, and will likely depend on the specific machine to which it is applied.

Regarding practical application of phase space tomography, it is worth mentioning that the requirements in terms of beamline design and diagnostics capability are

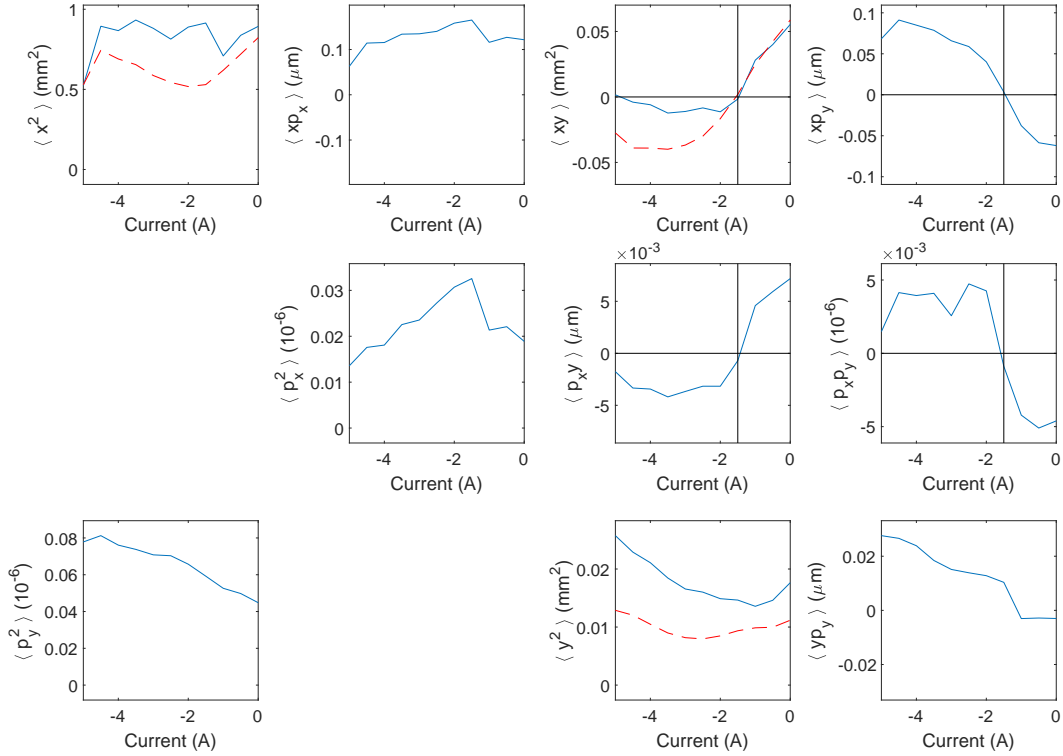


FIG. 12: Elements of the covariance matrix at SCR-02 (the Reconstruction Point) as functions of current in the bucking coil. Blue solid lines show the values determined from four-dimensional phase space tomography; red dashed lines show the values calculated from the directly observed image of the beam on SCR-02. Note that in the case of the tomography analysis, the elements describing coupling between the transverse degrees of freedom (shown in the top right 2×2 block diagonal) vanish for a bucking coil current of approximately -1.5 A: this is consistent with the current at which the difference between the normal mode emittances is minimised (as shown in Fig. 10).

not demanding. In CLARA FE, the diagnostics section consists of a short (1.661 m) section of beamline between two transverse beam profile monitors, and containing three (adjustable strength) quadrupoles. The design of this section was developed before detailed plans were prepared for phase space tomography studies, and there is limited flexibility in optimising the phase advances and optical functions over the length of the diagnostics section. Nevertheless, it was possible to identify sets of quadrupole strengths to provide the observations necessary for the analysis and results presented here.

So far, we have used an algebraic reconstruction technique for the phase space tomography. This technique has the advantage (compared to other tomography algorithms) of ease of implementation and flexibility in terms of the input data. However, it is possible that different algorithms may provide better (more accurate, or more detailed) results, and we hope to explore the possible benefits and limitations of alternative tomography methods. A particular issue with tomography in four-dimensional phase space is the demand on computer memory for processing the data and storing the results, especially at high resolution in phase space. However, because of the nature of the problem, the memory requirements will almost inevitably scale with the fourth power of the phase space

resolution, and it seems unlikely that other tomography methods would provide significant benefit in this respect. It is possible that more sophisticated computational techniques may allow some reduction in the memory requirements for a given resolution, e.g. [30].

While improvements and refinements in the technique are planned, the results so far show that four-dimensional phase space tomography is a useful technique for detailed beam characterisation and for machine tuning and optimisation. It is hoped that further studies will include investigation of space-charge effects in the electron source and beam dynamics effects (such as wake fields) in the linac.

Acknowledgments

We would like to thank our colleagues in STFC/ASTeC at Daresbury Laboratory for help and support with various aspects of the simulation and experimental studies of CLARA FE.

This work was supported by the Science and Technology Facilities Council, UK, through a grant to the Cockcroft Institute.

- [1] H. Wiedemann, *Particle Accelerator Physics*, (Third edition, Springer-Verlag, New York, 2007), pp. 164–166.
- [2] M.G. Minty and F. Zimmermann, *Measurement and Control of Charged Particle Beams, Particle Acceleration and Detection*, (Springer, Berlin, 2003). ISBN 978-3-662-08581-3
- [3] C.B. McKee, P.G. O’Shea, J.M.J. Madey, “Phase space tomography of relativistic electron beams”, *Nuclear Instruments and Methods in Physics Research Section A*, **358** (1995), pp. 264–267.
- [4] V. Yakimenko, M. Babzien, I. Ben-Zvi, R. Malone and X.-J. Wang, “Electron beam phase-space measurement using a high-precision tomography technique”, *Phys. Rev. ST Accel. Beams* **9**, 112801 (2006).
- [5] D. Stratakis, R.A. Kishek, H. Li, S. Bernal, M. Walter, B. Quinn, M. Reiser and P.G. O’Shea, “Tomography as a diagnostic tool for phase space mapping of intense particle beams”, *Phys. Rev. ST Accel. Beams* **6**, 122801 (2003).
- [6] D. Stratakis, K. Tian, R.A. Kishek, I. Haber, M. Reiser and P.G. O’Shea, “Tomographic phase-space mapping of intense particle beams using solenoids”, *Physics of Plasmas* **14**, 120703 (2007).
- [7] Dao Xiang, Ying-Chao Du, Li-Xin Yan, Ren-Kai Li, Wen-Hui Huang, Chuan-Xiang Tang, and Yu-Zheng Lin, “Transverse phase space tomography using a solenoid applied to a thermal emittance measurement”, *Phys. Rev. ST Accel. Beams* **12**, 022801 (2009).
- [8] Michael Röhrs, Christopher Gerth, Holger Schlarb, Bernhard Schmidt, and Peter Schmüser, “Time-resolved electron beam phase space tomography at a soft x-ray free-electron laser”, *Phys. Rev. ST Accel. Beams* **12**, 050704 (2009).
- [9] Q.Z. Xing, L. Du, X.L. Guan, C.X. Tang, M.W. Wang, X.W. Wang and S.X. Zheng, “Transverse profile tomography of a high current proton beam with a multi-wire scanner”, *Phys. Rev. Accel. Beams* **21**, 072801 (2018).
- [10] Fuhao Ji, Jorge Giner Navarro, Pietro Musumeci, Daniel B. Durham, Andrew M. Minor and Daniele Filippetto, “Knife-edge based measurement of the 4D transverse phase space of electron beams with picometer-scale emittance”, *Phys. Rev. Accel. Beams* **22**, 082801 (2019).
- [11] J.A. Clarke et al., *CLARA Conceptual Design Report*, (STFC, Daresbury, Warrington, UK, 2013).
- [12] D. Angal-Kalinin et al., “Status of CLARA Front End commissioning and first user experiments”, *Proceedings of IPAC2019, Melbourne, Australia* (2019), pp. 1851–1854.
- [13] A. Friedman, D.P. Grote, C.M. Celata, J.W. Staples, “Use of projectional phase space data to infer a 4D particle distribution”, *Laser and Particle Beams*, **21**(1) (2003), pp. 17–20.
- [14] K.M. Hock and A. Wolski, “Tomographic reconstruction of the full 4D transverse phase space”, *Nuclear Instruments and Methods in Physics Research Section A*, **726** (2013), pp. 8–16.
- [15] Lianmin Zheng, Jiahang Shao, Yingchao Du, John G. Power, Eric E. Wisniewski, Wanming Liu, Charles E. Whiteford, Manoel Conde, Scott Doran, Chunguang Jing, Chuanxiang Tang and Wei Gai, “Experimental demonstration of the correction of coupled-transverse-dynamics aberration in an rf photoinjector”, *Phys. Rev. Accel. Beams* **22**, 072805 (2019).
- [16] K.M. Hock, M.G. Ibison, D.J. Holder, A. Wolski and B.D. Muratori, “Beam tomography in transverse normalised phase space”, *Nuclear Instruments and Methods in Physics Research Section A*, **642** (2011), pp. 36–44.
- [17] A. Wolski, “Alternative approach to general coupled linear optics”, *Phys. Rev. ST Accel. Beams* **9**, 024001 (2006).
- [18] D. Angal-Kalinin et al., “Commissioning of Front End of CLARA facility at Daresbury Laboratory”, *Proceedings of IPAC2018, Vancouver, BC, Canada* (2018), pp. 4426–4429.
- [19] Pulsar Physics, the General Particle Tracer (GPT) code. <http://www.pulsar.nl/gpt>
- [20] S.B. van der Geer, O.J. Luiten, M.J. de Loos, G. Pöplau, U. van Rienen, “3D space-charge model for GPT simulations of high brightness electron bunches”, *Institute of Physics Conference Series*, No. 175 (2005), p. 101. ISBN 0-7503-0939-3
- [21] Gisela Pöplau, Ursula van Rienen, Bas van der Geer, and Marieke de Loos, “Multigrid algorithms for the fast calculation of space-charge effects in accelerator design”, *IEEE Transactions on Magnetics*, Vol 40, No. 2 (2004), p. 714.
- [22] P. Raimondi, P.J. Emma, N. Toge, N.J. Walker and V. Ziemann, “Sigma matrix reconstruction in the SLC final focus”, *Proceedings of the Particle Accelerator Conference (PAC93)*, Washington, D.C., USA (1993), pp. 98–99.
- [23] E. Prat and M. Aiba, “Four-dimensional transverse beam matrix measurement using the multiple-quadrupole scan technique”, *Phys. Rev. ST Accel. Beams* **17**, 052801 (2014).
- [24] M.D. Woodley and P. Emma, “Measurement and correction of cross-plane coupling in transport lines”, *Proceedings of the 20th International Linac Conference*, Monterey, CA, USA (2000), pp. 196–198.
- [25] A.C. Kak and Malcolm Slaney, “Principles of Computerized Tomographic Imaging”, *Society of Industrial and Applied Mathematics* (2001). ISBN 978-0-89871-494-4
- [26] G. Minerbo, “MENT: a maximum entropy algorithm for reconstructing a source from projection data”, *Computer Graphics and Image Processing*, **10** (1979).
- [27] C.T. Mottershead, “Maximum entropy beam diagnostic tomography”, *IEEE Transactions on Nuclear Science*, NS-32, 5 (1985), pp. 1970–1972.
- [28] Y. Derbenev, “Adapting optics for high energy electron cooling”, *Tech. Rep. UM HE 98–04*, Randall Laboratory of Physics, University of Michigan, Ann Arbor, MI, USA (1998).
- [29] R. Brinkmann, Y. Derbenev and K. Flöttmann, “A low emittance, flat-beam electron source for linear colliders”, *Phys. Rev. ST Accel. Beams* **4**, 053501 (2001).
- [30] I.C.S. Cosme, I.F. Fernandes, J.L. de Carvalho, S. Xavier-de-Souza, “Memory-usage advantageous block recursive matrix inverse”, *Applied Mathematics and Computation* **328** (2018), pp. 125–136.